

What Produces Dust Polarization in the HH 212 Protostellar Disk at 878 μm : Dust Self-Scattering or Dichroic Extinction?

Chin-Fei Lee^{1,2}, Zhi-Yun Li³, Haifeng Yang⁴, Zhe-Yu Daniel Lin³, Tao-Chung Ching^{5,6}, and Shih-Ping Lai^{7,1}

ABSTRACT

We report new dust polarization results of a nearly edge-on disk in the HH 212 protostellar system, obtained with ALMA at $\sim 0''.035$ (14 au) resolution in continuum at $\lambda \sim 878 \mu\text{m}$. Dust polarization is detected within ~ 44 au of the central source, where a rotationally supported disk has formed. The polarized emission forms V-shaped structures opening to the east and probably west arising from the disk surfaces and arm structures further away in the east and west that could be due to potential spiral arms excited in the outer disk. The polarization orientations are mainly parallel to the minor axis of the disk, with some in the western part tilting slightly away from the minor axis to form a concave shape with respect to the center. This tilt of polarization orientations is expected from dust self-scattering, e.g., by 50–75 μm grains in a young disk. The polarized intensity and polarization degree both peak near the central source with a small dip at the central source and decrease towards the edges. These decreases of polarized intensity and polarization degree are expected from dichroic extinction by grains aligned by poloidal fields, but may also be consistent with dust self-scattering if the grain size decreases toward the edges. It is possible that both

¹Academia Sinica Institute of Astronomy and Astrophysics, P.O. Box 23-141, Taipei 106, Taiwan; cflee@asiaa.sinica.edu.tw

²Graduate Institute of Astronomy and Astrophysics, National Taiwan University, No. 1, Sec. 4, Roosevelt Road, Taipei 10617, Taiwan

³Astronomy Department, University of Virginia, Charlottesville, VA 22904, USA

⁴Institute for Advanced Study, Tsinghua University, Beijing, 100084, People's Republic of China

⁵CAS Key Laboratory of FAST, National Astronomical Observatories, Chinese Academy of Sciences, People's Republic of China

⁶National Astronomical Observatories, Chinese Academy of Sciences, A20 Datun Road, Chaoyang District, Beijing 100012, People's Republic of China

⁷Institute of Astronomy and Department of Physics, National Tsing Hua University, Hsinchu, Taiwan

mechanisms are needed to produce the observed dust polarization, suggesting the presence of both grain growth and poloidal fields in the disk.

Subject headings: stars: formation — ISM: individual: HH 212 — ISM: accretion and accretion disk – ISM: magnetic fields – polarization

1. Introduction

HH 212 is a young accreting protostellar system with a highly collimated spinning jet (Zinnecker, McCaughrean, & Rayner 1998; Lee et al. 2017c) in the Class 0 phase in Orion at a distance of ~ 400 pc. With a nearly edge-on and vertically resolved disk (Lee et al. 2017a) deeply embedded in a dense rotating molecular core (Wiseman et al. 2001) and an infalling-rotating flattened envelope (Lee et al. 2006, 2014), it becomes a textbook case to study the disk formation and accretion process in the earliest phase of star formation. The disk is rotationally supported, surrounding a protostar with a mass of $\sim 0.25 M_{\odot}$ (Codella et al. 2014; Lee et al. 2017b). Dust polarization has been detected in the disk in submillimeter wavelength at $\sim 875 \mu\text{m}$ (Lee et al. 2018a), and it can be due to either dichroic extinction by grains aligned magnetically by poloidal fields or dust self-scattering by grains with a maximum size up to $100 \mu\text{m}$ in the outer disk. Both of these possibilities have important implications. If it is the former, then it means poloidal fields have been dragged into the outer disk and can play a role in both the disk evolution and the disk-wind launching (Konigl & Pudritz 2000). If it is the latter, then it means the grains have grown from $\sim 0.1 \mu\text{m}$ in the ISM to $100 \mu\text{m}$ in the outer disk, and this grain growth can facilitate an earlier start of planet formation in the earliest phase of star formation. Since the dust disk appears to be geometrically thick, the grain settling is not significant, possibly because of turbulence produced by an active accretion. Recent multi-wavelength continuum observations have shown that the disk is likely subject to gravitationally instability (Tobin et al. 2020), supporting that the disk is in an active accretion phase.

Recently, dust polarization due to aligned grains has also been detected on the larger scales in the dense molecular core and the flattened envelope around the disk, revealing magnetic field morphology there (Yen et al. 2021; Galametz et al. 2020), and thus allowing us to check the possible presence of poloidal fields in the outer disk. In the molecular core at a size scale of ~ 0.1 pc, the magnetic fields are found to be poloidal with a mean axis at a position angle of $\sim 35^{\circ} \pm 10^{\circ}$, slightly misaligned with the disk axis (of symmetry) by $\sim 12^{\circ}$ counterclockwise (see Figure 11 in Yen et al. 2021). Note that the disk axis has a position angle of $\sim 23^{\circ}$, well aligned with the jet axis (Lee et al. 2017a). In the flattened envelope at a size scale of ~ 1500 au, the magnetic fields are found to have a similar mean axis to

that in the molecular core (Galametz et al. 2020). Interestingly, the innermost flattened envelope with a size scale of ~ 500 au detected in dust continuum also has an axis with a similar position angle of $\sim 36^\circ \pm 10^\circ$ (see Figure 1c Lee et al. 2017a). This supports the notion that magnetic fields play an important role in the collapsing process of the molecular core and that the flattened envelope is a pseudo-disk formed by magnetically guided collapse (Hirano & Machida 2019). Similar pseudo-disks have also been detected in HH 211 (Lee et al. 2019b) and OMC-3/MMS6 (Liu 2020). In this scenario, the poloidal fields are dragged into the flattened envelope from the molecular core. These poloidal fields can then be dragged into the outer disk. Recent detection of disk wind from the outer disk (Tabone et al. 2017; Lee et al. 2018b; Tabone et al. 2020; Lee et al. 2021) also suggests a need for poloidal fields there.

The contribution of dust self-scattering to the continuum emission of this disk has also been briefly investigated recently. By modeling the continuum emission maps in 3 wavelengths (from 0.852 to 3 mm) simultaneously, Lin et al. (2021) found that a pure thermal dust emission can roughly reproduce the dust continuum in those wavelengths. This suggests that the dust self-scattering, even if present at submillimeter wavelength, could be relatively small in this disk. Similar conclusion was obtained in Galván-Madrid et al. (2018). Considering a maximum grain size of 60-150 μm estimated from scattering-induced polarization in Class I and II protostellar systems in the more evolved phases (Kataoka et al. 2016a; Yang et al. 2016a; Bacciotti et al. 2018; Hull et al. 2018), it is also reasonable to consider a maximum grain size smaller than 100 μm in HH 212 in the Class 0 phase.

In this paper, we present our new dust polarization detection in the HH 212 disk in continuum, obtained with Atacama Large Millimeter/submillimeter Array (ALMA) at 3 times higher resolution than previous observations, in order to further determine the contributions of dichroic extinction and dust self-scattering. By modeling the polarization morphology, polarized intensity, and polarization degree, we find that neither mechanisms can fully reproduce the observations individually and that both mechanisms might be required. Being edge-on and vertically resolved, the HH 212 disk provides the best view to search for poloidal fields and to study the grain growth and settling that are the crucial first steps towards planet formation.

2. Observations

Linear dust polarization observations of the HH 212 disk were obtained with ALMA in Band 7 in Cycle 5 (Project ID: 2017.1.00044.S). Three observations were taken on 2017 November 27, with a total time of ~ 98 minutes on the target. A single pointing was used

to map the disk with a primary beam of $\sim 17''$. 47 antennas were used in the observations, with projected baselines of ~ 60 –8500 m. The maximum recoverable size scale was $\sim 0''.4$, enough to map the disk without any significant missing flux. The correlator was set up to have 4 spectral windows (centered at 334.7, 336.5, 346.6, and 348.4 GHz, respectively), with a total bandwidth of ~ 8 GHz centered at ~ 341.5 GHz (or $878 \mu\text{m}$ correspondingly).

The Common Astronomy Software Applications (CASA) package was used to calibrate the uv data manually by the ALMA QA2 team, with quasar J5010+1800 as a passband and flux calibrator, and quasar J0541-0211 as a gain calibrator, and quasar J0522-3627 as a polarization calibrator. We adopted a super-uniform weighting with a robust factor of 0.5 (with $\text{npixels}=0$) for the uv data to generate the continuum map of the disk at ~ 341.5 GHz with a synthesized beam (resolution) of $\sim 0''.036 \times 0''.032$. We also performed a phase-only self-calibration using the continuum intensity (Stokes-I) map to improve the map fidelity. In Stokes I map, the noise level is $\sigma \sim 25 \mu\text{Jy beam}^{-1}$ (or 0.233 K). In Stokes Q and U maps, the noise level is $\sigma_p \sim 19 \mu\text{Jy beam}^{-1}$ (or 0.177 K). From the Stokes parameters, we can derive the linear polarized intensity, polarization fraction, and polarization orientation. Linear polarized intensity is defined as $P_i = \sqrt{Q^2 + U^2 - \sigma_p^2}$ and thus bias-corrected. Then polarization fraction is defined as $P = P_i/I$. According to ALMA Technical Handbook in Cycle 5, the instrumental error on P is expected to be $\lesssim 0.2\%$ for the disk, which has a size much smaller than $1/3$ of the primary beam. Polarization orientations are defined by the E vectors.

3. Results

Throughout this paper, in order to facilitate our presentations, we rotate our maps by 23° clockwise to align the major axis of the disk in the horizontal direction. Figure 1 shows the maps from our polarization observations towards the disk in continuum at $\lambda \sim 878 \mu\text{m}$. As seen before at $\lambda \sim 852 \mu\text{m}$ in Lee et al. (2017a), the continuum intensity map shows a “hamburger” like emission structure for the disk, with a dark lane along the equatorial plane sandwiched by two brighter features arising from the upper and lower disk surfaces. As discussed in that paper, the brighter feature above is slightly brighter than the one below, because the nearside of the disk is tilted slightly to the south. In addition, the emission is mainly from the outer edge of the disk on the nearside, because of nearly edge-on orientation, large geometric thickness, and high optical depth of the disk.

Polarized emission has been detected before at a similar wavelength (Lee et al. 2018a). Now at 3 times higher resolution, we can clearly see that the polarized emission is mainly detected in the dark lane within the centrifugal barrier, which has a radius of $\sim 0''.11$ (44

au), where a rotationally supported disk has formed (Lee et al. 2017b). Interestingly, the polarized intensity shows two peaks in the midplane near the central source on either side at a distance of ~ 0.02 (8 au), with a small dip at the central source (see also Figure 2). The western peak (right) is brighter than the eastern peak. In addition, the polarized emission extending to the east also peaks near the two (upper and lower) disk surfaces, forming a V-shaped structure near the central source (delineated by the white dotted curve in Figure 1b) opening to the east, and then an arm structure further in the east near the midplane. The polarized emission extending to the west could also form such a V-shaped structure near the central source opening to the west, but observations at higher resolution are needed to resolve and confirm it. Nonetheless, it also shows an arm structure further in the west in the midplane. Since the disk is subject to gravitational instability (Tobin et al. 2020) and thus might have spiral arms as seen in the HH 111 disk (Lee et al. 2020), the polarization emission near and in the midplane could be affected by them, forming polarized arm structures there.

The polarization orientations (as indicated by the line segments) are rather uniform and mostly parallel to the disk minor axis, which is the axis perpendicular to the disk midplane. Going away from the midplane to the disk surfaces, the polarization orientations in the west are tilted slightly away from the minor axis to form a concave shape with respect to the center. The polarization degree peaks at $\sim 3\text{-}4\%$ near the center at the two polarized intensity peaks and decreases outwards along the major and minor axes to $\sim 1.5\%$ at the edges and surfaces of the disk (see also Figure 2). The polarized intensity further out drops below the 3σ sensitivity, as shown in Figure 2.

4. Polarization Models

In our previous study of dust polarization of this disk at similar wavelength at a lower resolution of $\sim 0''.12$ (Lee et al. 2018a), the morphology of the polarized emission was not resolved and the polarization could be due to either dichroic extinction by dust grains aligned by poloidal magnetic fields or dust self-scattering by large grains with a size as large as $100 \mu\text{m}$. Following up on that, we first introduce a simple parametrized disk model and then explore these two possible mechanisms in more details.

4.1. A Flared Dusty Disk Model

Similar flared disk models have been used to produce the thermal dust emission in this disk (Lee et al. 2017a; Galván-Madrid et al. 2018; Lin et al. 2021). Here we adopt a similar

model to reproduce the observed dust polarization. The disk is composed of dust and gas in vertical hydrostatic equilibrium with a scale height of h_s . In a cylindrical coordinate system, the disk is assumed to have the following dust mass density and temperature

$$\begin{aligned}\rho(R, z) &= \rho_t \left(\frac{R}{R_t}\right)^{-p} \exp\left(-\frac{z^2}{2h_s^2}\right) \\ T(R, z) &= T_t \left(\frac{R}{R_t}\right)^{-q} \exp\left(\frac{z^2}{2h_s^2}\right)\end{aligned}\quad (1)$$

where R_t is a reference radius to be defined below, ρ_t and T_t are the dust mass density and temperature in the disk midplane at R_t , respectively, and p and q are the power-law indexes. As in Lee et al. (2017a), we assume that $p = 2$ and $q = 0.75$. Assuming a gas to dust mass ratio of 100 and a gas composed of molecular hydrogen and atomic helium, we have the number density of molecular hydrogen at R_t given by

$$n_t = \frac{100 \rho_t}{1.4 m_{\text{H}_2}} \quad (2)$$

Here the number density of Helium is assumed to be 0.2 times that of molecular hydrogen.

The scale height is assumed to be proportional to $\frac{c_s}{v_\phi} R$, where c_s is the isothermal sound speed proportional to $T^{1/2}$ and thus to $R^{-q/2}$, and v_ϕ is the rotational velocity assumed to be Keplerian and thus proportional to $R^{-1/2}$ (Lee et al. 2017b). As a result, the scale height is given by

$$h_s(R) = h_t \left(\frac{R}{R_t}\right)^{1+(1-q)/2} \quad (3)$$

with h_t being the scale height at R_t . The total height of the disk can reach $\sqrt{2}h_s$. However, as discussed in Lee et al. (2017a), since the continuum emission of the disk becomes geometrically thinner near the outer edge, the total height of the disk is revised to

$$h_o(R) = \sqrt{2}h_s \begin{cases} 1 & \text{if } R < R_t, \\ \exp\left[-\left(\frac{R-R_t}{R_o-R_t}\right)^2\right] & \text{if } R_t \leq R \leq R_o \end{cases} \quad (4)$$

where R_o is the outer radius of the disk and R_t is the radius beyond which the total height of the disk is tapered to roughly match the observed height in the outer edge. Then the disk has a surface density of dust given by

$$\Sigma(R) = \int_{-h_o}^{h_o} \rho dz \quad (5)$$

Radiative transfer assuming LTE is used to calculate the dust emission from the model, using our radiative transfer code in Lee et al. (2017a). A major uncertainty in the model

is the dust absorption opacity. Recently, multiple-wavelength observations in longer wavelengths have been used to constrain it. Using the dust continuum emission at 0.87 and 9 mm at $\sim 0''.1$ resolution, Tobin et al. (2020) has found that the disk has Toomre Q values of 1–2.5. By modeling the continuum emission maps in 3 wavelengths (from 0.852 to 3 mm, including a wavelength similar to the observed here) simultaneously at higher resolution assuming pure thermal dust emission, Lin et al. (2021) have estimated the absorption opacity to be $\kappa_{\text{abs}} \sim 1.9 Q \text{ cm}^2$ per gram of dust at the wavelength of $\sim 852 \mu\text{m}$. Thus here in our model, adopting $Q \sim 1$, we assume $\kappa_{\text{abs}} \sim 1.9 \text{ cm}^2$ per gram of dust at the observed wavelength of $878 \mu\text{m}$. Dust self-scattering opacity will be added later when we study the contribution of dust self-scattering to the dust polarization.

The disk is assumed to be nearly edge-on with an inclination of $\sim 87^\circ$ (Lee et al. 2021) and the nearside tilted slightly to the south. By matching the observed structure of the continuum emission assuming pure dust thermal emission, we find that $R_t \sim 34 \pm 5 \text{ au}$ (or $0''.085 \pm 0''.013$), $R_o \sim 68 \pm 10 \text{ au}$ (or $0''.17 \pm 0''.03$), $h_s \sim 12 \pm 2 \text{ au}$ (or $0''.03 \pm 0''.005$), $\rho_t \sim 3.0 \pm 0.4 \times 10^{-15} \text{ g cm}^{-3}$ (or $n_t \sim 6.5 \pm 1.0 \times 10^{10} \text{ cm}^{-3}$), and $T_t \sim 65 \pm 10 \text{ K}$, consistent with those found in Lee et al. (2017a), but with a factor of 3 higher n_t due to a factor of 3 lower absorption opacity. Thus, the disk has a total (gas plus dust) mass of $\sim 0.14 \pm 0.02 M_\odot$, which is also about a factor of 3 higher than that derived in Lee et al. (2017a) and thus becomes $\sim 56\%$ of the protostellar mass. This mass is also consistent with that found by Galván-Madrid et al. (2018), who assumed a similar absorption opacity at $878 \mu\text{m}$ according to their adopted opacity law. This disk is so massive and thus subject to gravitational instability, as discussed in Tobin et al. (2020).

4.2. Dichroic Extinction by Magnetically Aligned Grains

Dichroic extinction is the differential attenuation of two orthogonal components of the E vector of light by magnetically aligned grains (Wood 1997), resulting in a net polarization of light. In this scenario, we assume that the disk is threaded with uniform (vertical) poloidal magnetic fields and the dust grains are aligned by the magnetic fields, with their long axis perpendicular to the field direction (Andersson et al. 2015). Because the bulk of the disk is optically thick at our observing wavelength and the temperature increases along the line of sight into the disk, dichroic extinction (rather than direct emission) by aligned grains is expected to determine the degree and orientation of the polarization relative to the magnetic field direction (see, e.g., Figure 1 in Lin et al. 2020, for an illustration).

Our radiative transfer code can be expanded to calculate the polarization maps. With an assumption of LTE, the radiative transfer in Stokes I , Q , and U parameters can be given

by the following (see also POLARIS in Reissl et al. 2016)

$$\frac{d}{\rho ds} \begin{pmatrix} I \\ Q \\ U \end{pmatrix} = - \begin{pmatrix} C_{\text{ext}} & C_{\text{pol}} \cos 2\psi & C_{\text{pol}} \sin 2\psi \\ C_{\text{pol}} \cos 2\psi & C_{\text{ext}} & 0 \\ C_{\text{pol}} \sin 2\psi & 0 & C_{\text{ext}} \end{pmatrix} \begin{pmatrix} I \\ Q \\ U \end{pmatrix} + B_\nu(T) \begin{pmatrix} C_{\text{ext}} \\ C_{\text{pol}} \cos 2\psi \\ C_{\text{pol}} \sin 2\psi \end{pmatrix} \quad (6)$$

The extinction cross section per gram (i.e., extinction opacity) and polarization cross section per gram (i.e., polarization opacity) can be given by (see Lee & Draine 1985)

$$\begin{aligned} C_{\text{ext}} &= \kappa_{\text{abs}} \left[1 - \alpha \left(\frac{\cos^2 \gamma}{2} - \frac{1}{3} \right) \right] \\ C_{\text{pol}} &= \alpha \kappa_{\text{abs}} \cos^2 \gamma \end{aligned} \quad (7)$$

where γ is the angle between the local \mathbf{B} vector and the plane of the sky, and $\psi = \phi + 90^\circ$ is the polarization angle measuring from the north (ordinate axis) to the east, with ϕ being the angle between the projection of the local \mathbf{B} vector on the plane of the sky and north. In order to calculate the polarization quantities, we assume a polarization efficiency α , which defines the maximum polarization fraction in an optically thin region (Fiege & Pudritz 2000; Padoan et al. 2001). After the integration along each line of sight, the resulting polarization intensity, fraction, and angle can then be given respectively by

$$P_i = \sqrt{Q^2 + U^2} \quad (8)$$

$$P = \frac{P_i}{I} \quad (9)$$

and

$$\psi = \frac{1}{2} \tan^{-1} \frac{U}{Q} \quad (10)$$

By matching the polarization fraction of ~ 0.03 observed in the optically thick central region of the disk, we find that a value of $\alpha \sim 0.075$ is required in the model. In this case, $C_{\text{ext}} \approx \kappa_{\text{abs}}$.

Figure 3 shows the model results. The total intensity map of the emission shows a dark lane along the major axis sandwiched by two brighter curved features above and below, because the midplane of the disk is cooler and optically thicker than the surfaces. Since the disk's nearside is tilted slightly to the south, the upper disk surface is slightly exposed and thus becomes brighter than the lower one. The whole disk is optically thick. In particular, the optical depth peaks at the center with a value greater than 100, and it decreases outward and drops to ~ 1 near the outer edges and outer disk surfaces. The emission in the disk is polarized. Along the major axis, the polarized intensity peaks at the center and decreases outward and drops to zero at $\sim 0''.11$ (44 au) where the optical

depth drops to 3–5, and then increases again in the optically thinner outer edges. The initial decrease of the polarization fraction with distance is physically reasonable since the fraction of polarization produced by dichroic extinction along high optical depth sight-lines is determined mainly by the temperature gradient along the line of sight (los), which is the highest toward the center. As the sightline moves towards the outer edge of the disk, both the optical depth and the (los) temperature gradient decrease, weakening the contribution of the dichroic extinction to the polarization relative to that of the dichroic emission. Going away from the midplane to the disk surfaces, the polarized intensity increases with the increasing distance and peaks near the disk surfaces where the temperature is higher, outlining the disk surfaces. Then the polarized intensity drops to zero at $\sim 0''.03$ (12 au) where the optical depth drops to 3–5, and then increases again in the optically thinner outer surfaces. As a result, when the optical depth drops to 3–5, the polarized intensity and the resulting polarization degree drop to zero, forming an elliptical polarization gap around the inner disk. Interior to the polarization gap in the inner optically thicker region, the polarization orientations are parallel to the poloidal field direction and thus the minor axis, because of the dichroic extinction and the temperature gradient, as discussed in Lee et al. (2018a) and Lin et al. (2020). Going across the polarization gap to the outer optically thinner region, the polarization orientations flip by 90° to be perpendicular to the poloidal field (and thus the minor axis) direction. In this outer region, direct emission by aligned grains is dominant.

Figure 4 shows the model results convolved to the observed beam to be compared with the observations. The total intensity map of the emission also shows a dark lane sandwiched by two brighter features, similar to that seen in the observations. The polarization gap can still be seen in the convolved map around the inner disk. Interior to the polarization gap, the polarized emission from the upper and lower disk surfaces merge and form a single elongated polarization structure in the dark lane, with hints of V-shaped structures opening to the east and west still discernible, although far less prominent compared to the unconvolved map. This polarization structure, although less clearly V-shaped, could correspond to that observed in the dark lane, which shows a V-shaped structure opening to the east and probably another one opening to the west. Note that we do not intend to reproduce the polarized arm structures, which could be affected by potential spiral arms, as discussed earlier. Both the polarized intensity and polarization degree of the beam convolved model peak at the center and decrease outward, also roughly similar to the observed trends. The polarization orientations are parallel to the minor axis, also similar to the observed orientations, except for those in the west near the disk surfaces where the observed orientations are tilted slightly away from the minor axis to form a concave shape with respect to the center. However, unlike the observations that show two polarized emission peaks near the central source with a small dip in between, only one single polarized emission peak is seen in the model toward

the central source.

In the model, the polarized intensity drops to zero in the polarization gap and then increases outside. Outside the polarization gap, although the polarized emission is much fainter than that inside, the polarized emission in the upper surface and outer disk above the 3σ sensitivity level (encompassed by the orange contour) in Figure 4b should still be detectable in the current observations, with a flip of the polarization orientation to be perpendicular to the minor axis. However, such an increase in polarized intensity and a flip of polarization orientation in the outer disk are not detected here. Thus, the polarization gap and the increase of polarized intensity around the disk predicted in this model might not exist in the observations but deeper observations are needed to check them.

4.3. Dust Self-Scattering by Submillimeter-Sized Grains

Dust self-scattering by large grains ($100 \mu\text{m}$ or larger) has been found to contribute significantly to the (sub)millimeter dust polarization in the protoplanetary disks in the later phase of star formation (Kataoka et al. 2015, 2016a; Yang et al. 2016a,b, 2017), as seen in the evolved disks in, e.g., HL Tau (Kataoka et al. 2017; Stephens et al. 2017), CW Tau and DG Tau (Bacciotti et al. 2018), HD 142527 (Ohashi et al. 2018), IM Lup (Hull et al. 2018), and HD163296 (Dent et al. 2019). It can also contribute to the dust polarization in the early phase in the protostellar disks if the dust grains have grown to $100 \mu\text{m}$ in size (Sadavoy et al. 2018a; Alves et al. 2018; Harris et al. 2018; Sadavoy et al. 2018b). Since the scattering opacity is still uncertain, we parametrize it by

$$\kappa_{\text{sca}} = \frac{\omega}{1 - \omega} \kappa_{\text{abs}} \quad (11)$$

where κ_{abs} is the absorption opacity and ω is the albedo defined as

$$\omega = \frac{\kappa_{\text{sca}}}{\kappa_{\text{abs}} + \kappa_{\text{sca}}} \quad (12)$$

This albedo can be linked to grain size. For example, with a size distribution of $n(a) \propto a^{-3.5}$ and a mixture of silicate, water ice, and organics, a maximum grain size of 10, 25, 50, 75, $100 \mu\text{m}$, Kataoka et al. (2015) estimated an albedo of $\sim 0, 0.036, 0.23, 0.50, 0.70$, respectively, at the observed wavelength of $870 \mu\text{m}$, although the exact values depend on grain properties (such as shape and composition), which are uncertain.

Since the disk here is young in the deeply embedded, actively accreting protostellar phase, the grain size is expected to be smaller than $100 \mu\text{m}$ (Galván-Madrid et al. 2018; Lin et al. 2021). Since the dust polarization morphology due to dust self-scattering does

not depend much on the actual size of the grains (as long as the grains are not too large compared to the observing wavelength) and the grain composition, we adopt an albedo of 0.5, or equivalently assume a scattering opacity the same as the absorption opacity, to study the dust self-scattering effect. For demonstration purpose, we first derive the dust scattering matrix with the Mie approximation using the optical constants of an amorphous silicate (amorphous pyroxene with 70 percent magnesium and 30 percent iron) (Jaeger et al. 1994; Dorschner et al. 1995), a grain size of $100 \mu\text{m}$, and material density of 1.675 g cm^{-3} (Birnstiel et al. 2018), and then scale it down to have a scattering opacity the same as that of the absorption opacity to be consistent with our adopted albedo. Then we use the RADMC-3D¹ code (Dullemond et al. 2012) to produce the polarization maps. Since the dust-scattering opacity adds an additional optical depth and thus an attenuation of the dust emission, a higher temperature with $T_{\text{t}} \sim 95 \pm 14 \text{ K}$, which is about 50% higher than that without dust scattering, is required to roughly match the observed brightness temperature.

Figure 5 shows the model results. Like the dichroic extinction model, the total intensity map also shows a dark lane in the major axis sandwiched by two brighter features arising from the disk surfaces. The dark lane is wider because of a larger optical depth and the emission is scattered away from the midplane. However, unlike the dichroic extinction model, no polarization gap is seen. In addition, the polarized intensity shows a dip at the center because the radiation is most symmetric about the center. It increases outwards in all directions and peaks near the edges and at the disk surfaces, because of the increase of asymmetry and also the increase of temperature for the disk surfaces. It then drops rapidly to zero at the edges and above the surfaces. Like the total intensity, the polarized intensity from the upper disk surface is brighter than that from the lower one. The polarization degree also shows a similar trend to the polarized intensity, except near the two edges where the polarization degree continues to increase towards the edges due to the faster decrease of total intensity. The polarization orientations are parallel to the minor axis near the midplane and then tilted slightly away from the minor axis to form a concave shape with respect to the center when going away from the midplane to the upper and lower disk surfaces.

Figure 6 shows the model results convolved to the observed beam. The total intensity map shows a similar structure to that observed. The polarization orientations are mostly parallel to the minor axis, and tilted slightly away from the minor axis to form a concave shape with respect to the center when going away from the midplane to the disk surfaces, similar to that seen in the observations. Unlike the dichroic extinction model, the upper disk and lower disk surfaces in the polarization intensity do not merge to form a single elongated

¹RADMC-3D is a publicly available code for radiative calculations available at <http://www.ita.uni-heidelberg.de/~dullemond/software/radmc-3d/>

structure, because the dark lane is wider and the lower disk surface is much fainter. In addition, unlike those seen in the observations, the polarized intensity and polarization degree in the model increase toward the edges along the major axis and drop rapidly at the edges. With the polarized intensity peaks near the two edges, the resulting polarized intensity dip is much wider than the observed, inconsistent with the observations. We have tried with a smaller albedo of 0.25. In this case, the polarized emissions from the upper disk and lower disk surfaces move slightly closer to the midplane, forming V-shaped structures opening to the east and west, roughly similar to the observed. However, the polarized intensity still peaks at the two edges, inconsistent with the observations. Moreover, the polarization intensity becomes everywhere lower than the 3σ sensitivity limit in our current observations.

5. Discussion

Dust polarization is detected in the HH 212 disk within the centrifugal barrier at ~ 44 au, where a rotationally supported disk has formed. The comparison of our simple models with the observations suggests that neither a simple dichroic extinction model by magnetically aligned grains nor a simple dust self-scattering model can fully account for the observed polarization morphology, polarized intensity, and polarization degree simultaneously. The dichroic extinction model can produce an elongated polarized structure in the dark lane, with hints of V-shaped structures opening to the east and west, similar to the observations. It can also produce the decrease of polarized intensity and polarization degree in the dark lane from the center towards the edges. However, it can not produce a small polarized intensity dip at the center. In addition, it produces a polarization gap and polarized emission with polarization orientations perpendicular to the minor axis outside the gap in the outer disk, which are not seen in the observations. Also, it can not produce the observed slight tilt of polarization orientations away from the minor axis in the western part of the disk above and below the disk midplane. On the other hand, the dust self-scattering model can roughly produce the observed polarization orientations. However, it can not produce the observed decrease of polarized intensity and polarization degree from the center to the outer edges. Moreover, the polarized intensity in the model always peaks near the two edges, producing a dip much wider than the observed. Adding a flattened envelope around the disk may reduce the polarized intensity near the edges by shining radiation into the disk, but may not be sufficient to reduce it down to zero.

None of our two simple models can reproduce the small observed dip of polarized intensity towards the central source position. This polarized intensity dip is unlikely to be a

polarization hole due to depolarization of unresolved complicated polarization orientations, as seen in, e.g., Serpens SMM1 (Hull et al. 2017), because the polarization orientations there are rather uniform. Our dichroic extinction model assumes a constant polarization efficiency and thus grain alignment efficiency. A decrease of grain alignment efficiency toward the center, as proposed to explain the decrease of polarization fraction toward the region with higher column density (Galametz et al. 2018), may help to produce a small polarized intensity dip at the center. However, further work is needed to study this possibility. On the other hand, our self-scattering model assumes a single albedo and thus the same maximum grain size all over the disk. It is possible that the maximum grain size may decrease from the inner to the outer disk, as expected if the grain size increases across the centrifugal barrier from the outer disk to the inner disk. For example, the grains newly accreted from the envelope to the outer disk may be too small to scatter (sub)millimeter photons efficiently. Further modeling is needed to check if the decrease of maximum grain size toward the edges can produce a small polarized intensity dip at the center and a decrease of polarized intensity towards the edges.

It is also possible that both mechanisms contribute to the dust polarization in the HH 212 disk. The dichroic extinction model better produces the decrease of polarized intensity and polarization degree in the dark lane towards the edges, while scattering model better produces the tilt of the polarization orientations away from the minor axis when going away from the midplane to the disk surfaces. In addition, combining these two models may also produce two polarized intensity peaks near the central source with a small polarization dip at the central source, as seen in the observation. Since RADMC-3D cannot treat scattering by aligned (non-spherical) grains at the present time, we will defer the combined modeling to a future publication. As mentioned in the introduction, poloidal fields can be dragged from the dense molecular core into the innermost part of the envelope and then to the outer disk. If this is the case, the magnetic fields may be responsible for launching the rotating SO/SO₂ outflow extending out from the disk (Tabone et al. 2017; Lee et al. 2018b, 2021). Observations at higher resolution are needed to determine the location of the magnetic fields more accurately. Also as mentioned in the introduction, recent multi-wavelength observations suggested that the dust self-scattering contribution to the dust continuum emission should be smaller than the thermal dust emission (Lin et al. 2021), otherwise the required temperature in the disk would be too high. As seen in our model with an albedo $\omega = 0.5$, the temperature in the disk is already $\sim 50\%$ higher than that without dust scattering. According to Kataoka et al. (2015), albedos are 0.23, 0.50, and 0.70 for maximum grain sizes of 50, 75, and 100 μm , respectively, which then result in $\kappa_{\text{sca}} = 0.23, 1.0, \text{ and } 2.33 \kappa_{\text{abs}}$, respectively. Thus, in order to have a scattering opacity comparable to or smaller than the absorption opacity, the grains can have a maximum size of 50–75 μm , which is reasonable for a Class 0 disk in the outer

edges. Moreover, since the disk is vertically extended, the grain settling is unlikely to have taken place significantly. Hence, the grains are likely relatively small. Furthermore, smaller grains are better for magnetic alignment.

We can estimate whether the midplane temperature inferred from our modeling can be produced by viscous heating due to disk accretion. Since the disk here is optically thick, the midplane temperature due to viscous heating would be (Shakura & Sunyaev 1973)

$$T_{\text{mid}}(R) \sim \tau_{\text{R}}^{1/4} T_{\text{eff}}(R) \quad (13)$$

where T_{eff} is the effective (surface) temperature of the disk at $\tau \sim 1$ given by

$$T_{\text{eff}}(R) \sim \left(\frac{3GM\dot{M}}{8\pi\sigma R^3} \right)^{1/4} \quad (14)$$

and τ_{R} is the Rosseland mean optical depth defined as

$$\tau_{\text{R}} \equiv \frac{1}{2} \Sigma \kappa_{\text{R}} \quad (15)$$

with σ here being the Stefan Boltzmann constant, κ_{R} being the Rosseland mean opacity per gram of dust, and Σ being the surface density of dust. In HH 212, with $M \sim 0.25 M_{\odot}$ (Codella et al. 2014; Lee et al. 2014, 2017b) and $\dot{M} \sim 5 \times 10^{-6} M_{\odot} \text{ yr}^{-1}$ (Lee et al. 2014), we have $T_{\text{eff}} \sim 20$ K at R_{t} or 34 au. In our model, the dust surface density $\Sigma \sim 1.14 \text{ g cm}^{-2}$ at R_{t} . For a disk temperature between 20 and 100 K at that radius, the black-body radiation peaks at wavelength $\lambda_{\text{peak}} \sim 29 - 145 \mu\text{m}$, according to the Wien’s displacement law. Then, assuming a maximum grain size of 100 μm and judging from Figure 1 in Kataoka et al. (2015) that shows the dust opacity versus wavelength, we have $\kappa_{\text{R}} < 200 \text{ cm}^2 \text{ g}^{-1}$ and thus $\tau_{\text{R}} < 114$. Thus, the midplane temperature in the disk should be less than 65 K at R_{t} . Additional heating can come from irradiation by the central stellar object, so the midplane temperature of about 65 K at R_{t} inferred in our dichroic extinction model appears reasonable. We refrain from a detailed modeling of the temperature structure because it depends on the dust opacities, which are uncertain. Nevertheless, a midplane temperature of ~ 95 K at R_{t} as in our dust self-scattering model would require a Rosseland mean opacity of ~ 5 times higher and is thus too high.

6. Conclusions

We have resolved the dust polarization in the HH 212 disk in continuum at $\lambda \sim 878 \mu\text{m}$ and found it to be mainly arisen within the centrifugal barrier at ~ 44 au, where a rotationally supported disk has formed. The polarized intensity forms V-shaped structures

opening to the east and probably west arising from the disk surfaces and arm structures further away in the east and west. The polarization orientations are mainly parallel to the minor axis, with some in the western part tilting slightly away from the minor axis to form a concave shape with respect to the center when going away from the midplane to the upper and lower disk surfaces. The polarized intensity and polarization degree both peak near the central source with a small dip at the central source and decrease towards the disk outer edges. The observed tilt of the polarization orientations away from the minor axis is more consistent with that expected from dust self-scattering by $50\text{--}75\ \mu\text{m}$ grains, but the observed decreases of polarized intensity and polarization degree from the center to the edges are more consistent with those expected from dichroic extinction by grains aligned by poloidal fields. The decreases of polarized intensity and polarization degree toward the edges may also be consistent with dust self-scattering if the grain size decreases toward the edges, as expected if the grain size increases across the centrifugal barrier from the outer edges. It is possible that both mechanisms are needed to produce the observed dust polarization, suggesting the presence of both poloidal fields and grain growth in the disk. In addition, the polarized arm structures could be due to potential spiral arms excited in the outer disk as the disk has been found to be gravitational unstable.

We thank the anonymous referee for insightful comments. C.-F.L. thanks S.-Y. Liu for fruitful discussions on dust polarization due to magnetically aligned grains and H. B. Liu for fruitful discussions on grain growth and dust opacity. This paper makes use of the following ALMA data: ADS/JAO.ALMA# 2017.1.00044.S. ALMA is a partnership of ESO (representing its member states), NSF (USA) and NINS (Japan), together with NRC (Canada), MoST and ASIAA (Taiwan), and KASI (Republic of Korea), in cooperation with the Republic of Chile. The Joint ALMA Observatory is operated by ESO, AUI/NRAO and NAOJ. C.-F.L. acknowledges grants from the Ministry of Science and Technology of Taiwan (MoST 107-2119-M-001-040-MY3) and the Academia Sinica (Investigator Award AS-IA-108-M01). ZYL is supported in part by NASA 80NSSC18K1095 and 80NSSC20K0533 and NSF AST-1815784. Z. Lin acknowledges support by an ALMA SOS award and Jefferson Graduate Fellowship at the University of Virginia.

REFERENCES

- Alves, F. O., Girart, J. M., Padovani, M., et al. 2018, *A&A*, 616, A56. doi:10.1051/0004-6361/201832935
- Andersson, B.-G., Lazarian, A., & Vaillancourt, J. E. 2015, *ARA&A*, 53, 501

- Bacciotti, F., Girart, J. M., Padovani, M., et al. 2018, *ApJ*, 865, L12. doi:10.3847/2041-8213/aadf87
- Birnstiel, T., Dullemond, C. P., Zhu, Z., et al. 2018, *ApJ*, 869, L45. doi:10.3847/2041-8213/aaf743
- Codella, C., Cabrit, S., Gueth, F., et al. 2014, *A&A*, 568, L5
- Dent, W. R. F., Pinte, C., Cortes, P. C., et al. 2019, *MNRAS*, 482, L29. doi:10.1093/mnrasl/sly181
- Dorschner, J., Begemann, B., Henning, T., et al. 1995, *A&A*, 300, 503
- Dullemond, C. P., Juhasz, A., Pohl, A., et al. 2012, *Astrophysics Source Code Library*. ascl:1202.015
- Fiege, J. D. & Pudritz, R. E. 2000, *ApJ*, 544, 830. doi:10.1086/317228
- Galametz, M., Maury, A., Girart, J. M., et al. 2018, *A&A*, 616, A139. doi:10.1051/0004-6361/201833004
- Galametz, M., Maury, A., Girart, J. M., et al. 2020, *A&A*, 644, A47. doi:10.1051/0004-6361/202038854
- Galván-Madrid, R., Liu, H. B., Izquierdo, A. F., et al. 2018, *ApJ*, 868, 39
- Harris, R. J., Cox, E. G., Looney, L. W., et al. 2018, *ApJ*, 861, 91. doi:10.3847/1538-4357/aac6ec
- Hirano, S. & Machida, M. N. 2019, *MNRAS*, 485, 4667. doi:10.1093/mnras/stz740
- Hull, C. L. H., Mocz, P., Burkhart, B., et al. 2017, *ApJ*, 842, L9. doi:10.3847/2041-8213/aa71b7
- Hull, C. L. H., Yang, H., Li, Z.-Y., et al. 2018, *ApJ*, 860, 82. doi:10.3847/1538-4357/aabfeb
- Jaeger, C., Mutschke, H., Begemann, B., et al. 1994, *A&A*, 292, 641
- Kataoka, A., Tsukagoshi, T., Pohl, A., et al. 2017, *ApJ*, 844, L5
- Kataoka, A., Muto, T., Momose, M., Tsukagoshi, T., & Dullemond, C. P. 2016a, *ApJ*, 820, 54
- Kataoka, A., Tsukagoshi, T., Momose, M., et al. 2016b, *ApJ*, 831, L12

- Kataoka, A., Muto, T., Momose, M., et al. 2015, *ApJ*, 809, 78
- Konigl, A., & Pudritz, R. E. 2000, *Protostars and Planets IV*, 759
- Lee, H. M. & Draine, B. T. 1985, *ApJ*, 290, 211. doi:10.1086/162974
- Lee, C.-F., Ho, P. T. P., Beuther, H., Bourke, T. L., Zhang, Q., Hirano, N., & Shang, H. 2006, *ApJ*, 639, 292
- Lee, C.-F., Hirano, N., Zhang, Q., et al. 2014, *ApJ*, 786, 114
- Lee, C.-F., Ho, P. T. P., Li, Z.-Y., et al. 2017c, *Nature Astronomy*, 1, 0152
- Lee, C.-F., Li, Z.-Y., Ho, P. T. P., et al. 2017b, *ApJ*, 843, 27
- Lee, C.-F., Li, Z.-Y., Ho, P. T. P., et al. 2017a, *Science Advances*, 3, e1602935
- Lee, C.-F., Li, Z.-Y., Ching, T.-C., et al. 2018a, *ApJ*, 854, 56. doi:10.3847/1538-4357/aaa769
- Lee, C.-F., Li, Z.-Y., Codella, C., et al. 2018b, *ApJ*, 856, 14. doi:10.3847/1538-4357/aaae6d
- Lee, C.-F., Codella, C., Li, Z.-Y., et al. 2019a, *ApJ*, 876, 63
- Lee, C.-F., Kwon, W., Jhan, K.-S., et al. 2019b, *ApJ*, 879, 101. doi:10.3847/1538-4357/ab2458
- Lee, C.-F., Li, Z.-Y., & Turner, N. J. 2020, *Nature Astronomy*, 4, 142. doi:10.1038/s41550-019-0905-x
- Lee, C.-F., Tabone, B., Cabrit, S., et al. 2021, *ApJ*, 907, L41. doi:10.3847/2041-8213/abda38
- Lin, Z.-Y. D., Lee, C.-F., Li, Z.-Y., et al. 2021, *MNRAS*, 501, 1316. doi:10.1093/mnras/staa3685
- Lin, Z.-Y. D., Li, Z.-Y., Yang, H., et al. 2020b, *MNRAS*, 493, 4868. doi:10.1093/mnras/staa542
- Liu, H. B. 2020, arXiv:2010.05392
- Ohashi, S., Kataoka, A., Nagai, H., et al. 2018, *ApJ*, 864, 81. doi:10.3847/1538-4357/aad632
- Padoan, P., Goodman, A., Draine, B. T., et al. 2001, *ApJ*, 559, 1005. doi:10.1086/322504
- Reissl, S., Wolf, S., & Brauer, R. 2016, *A&A*, 593, A87. doi:10.1051/0004-6361/201424930

- Sadavoy, S. I., Myers, P. C., Stephens, I. W., et al. 2018b, *ApJ*, 869, 115. doi:10.3847/1538-4357/aaef81
- Sadavoy, S. I., Myers, P. C., Stephens, I. W., et al. 2018a, *ApJ*, 859, 165. doi:10.3847/1538-4357/aac21a
- Shakura, N. I. & Sunyaev, R. A. 1973, *A&A*, 500, 33
- Stephens, I. W., Yang, H., Li, Z.-Y., et al. 2017, *ApJ*, 851, 55. doi:10.3847/1538-4357/aa998b
- Tabone, B., Cabrit, S., Bianchi, E., et al. 2017, *A&A*, 607, L6. doi:10.1051/0004-6361/201731691
- Tabone, B., Cabrit, S., Pineau des Forêts, G., et al. 2020, *A&A*, 640, A82. doi:10.1051/0004-6361/201834377
- Tobin, J. J., Sheehan, P. D., Megeath, S. T., et al. 2020, *ApJ*, 890, 130
- Wiseman, J., Wootten, A., Zinnecker, H., & McCaughrean, M. 2001, *ApJ*, 550, L87
- Wood, K. 1997, *ApJ*, 477, L25. doi:10.1086/310518
- Yang, H., Li, Z.-Y., Looney, L. W., et al. 2016a, *MNRAS*, 460, 4109
- Yang, H., Li, Z.-Y., Looney, L., & Stephens, I. 2016b, *MNRAS*, 456, 2794
- Yang, H., Li, Z.-Y., Looney, L. W., Girart, J. M., & Stephens, I. W. 2017, *MNRAS*, 472, 373
- Yen, H.-W., Koch, P. M., Hull, C. L. H., et al. 2021, *ApJ*, 907, 33. doi:10.3847/1538-4357/abca99
- Zinnecker, H., McCaughrean, M. J. & Rayner, J. T. 1998, *Natur*, 394, 862

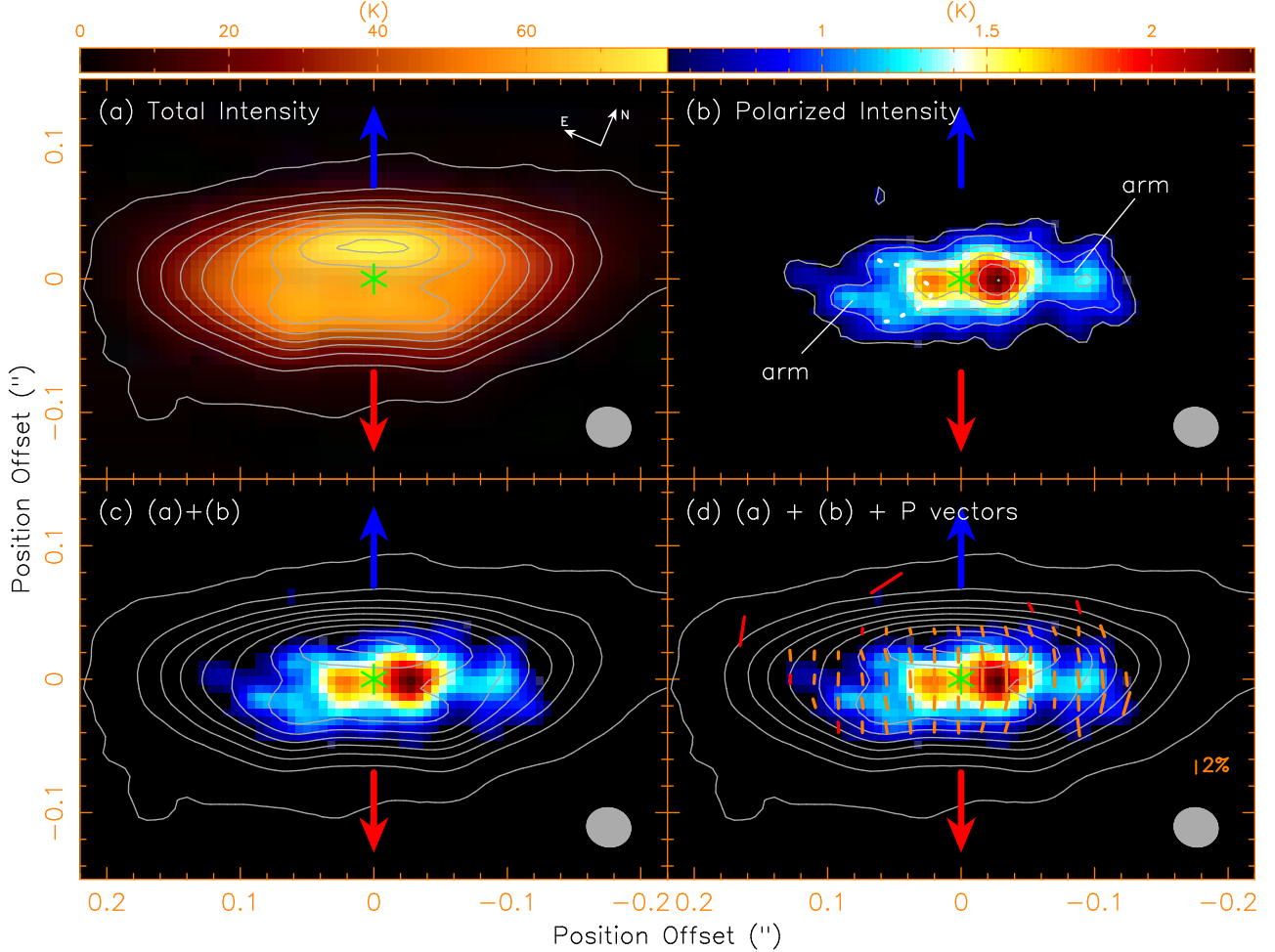


Fig. 1.— Polarization observations towards the HH 212 disk in continuum at $\lambda \sim 878 \mu\text{m}$ at $\sim 0''.036 \times 0''.032$ resolution. The blue and red arrows show the approaching and receding sides of the jet axis, respectively. The asterisk marks the possible position of the central source, which is assumed to have a coordinate $5^{\text{h}}43^{\text{m}}51^{\text{s}}.4086$ and $-1^{\circ}2'53''.154$, after comparing the total intensity maps between the observations and models discussed in the text. (a) Total intensity map. Contours start at 10σ with a step of 40σ , where $\sigma = 0.256 \text{ K}$. (b) Polarized intensity map. Contours start at $3 \sigma_p$ with a step of $2 \sigma_p$, where $\sigma_p = 0.173 \text{ K}$. (c) Total intensity (contours) and polarized intensity (color) maps. (d) Total intensity (contours), polarized intensity (color) maps and polarization orientations (line segments, red for detections of $(2.5 - 3)\sigma_p$ and cyan for detections greater than $3\sigma_p$).

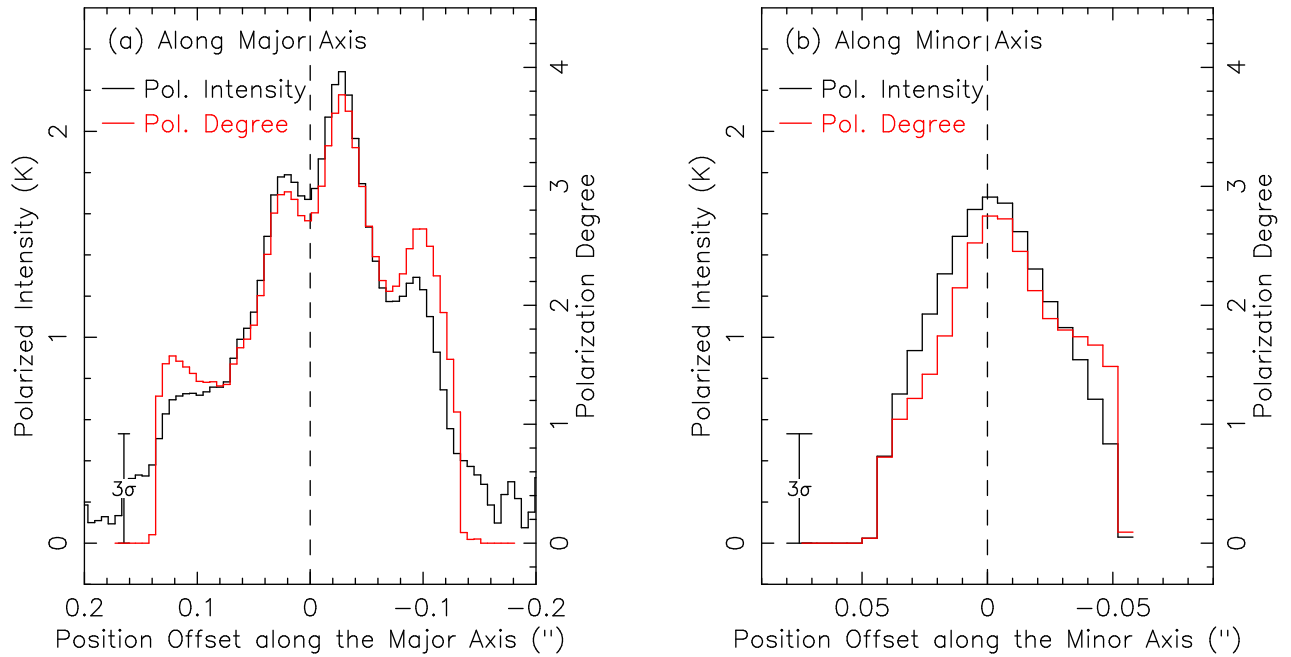


Fig. 2.— Polarized intensity (red curves) and polarization degree (black curves) at different position offsets from the central protostar along the (a) major and (b) minor axes.

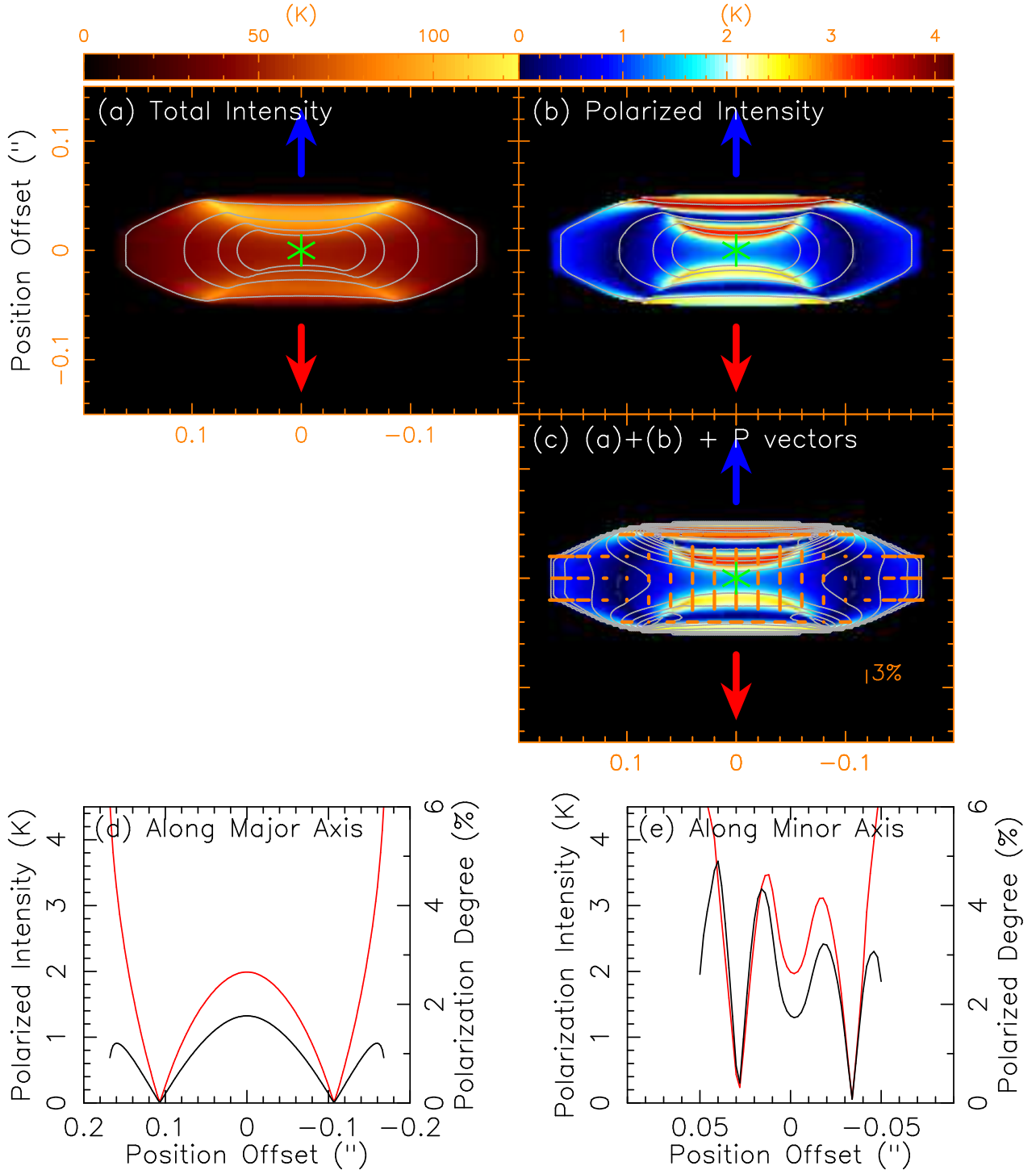


Fig. 3.— Dichroic extinction model by grains aligned magnetically by poloidal fields. (a) Total intensity map (color) with optical depth (contours). Contours start from 1 with a step of 3. Only first 4 contours are plotted. (b) Polarized intensity map (color) with optical depth (contours). (c) Total intensity map (contours), polarized intensity (color), and polarization degrees (line segments with the length for the degrees). (d) Polarized intensity (black curve) and polarization degree (red curve) along the major axis of the disk. (e) Polarized intensity (black curve) and polarization degree (red curve) along the minor axis of the disk.

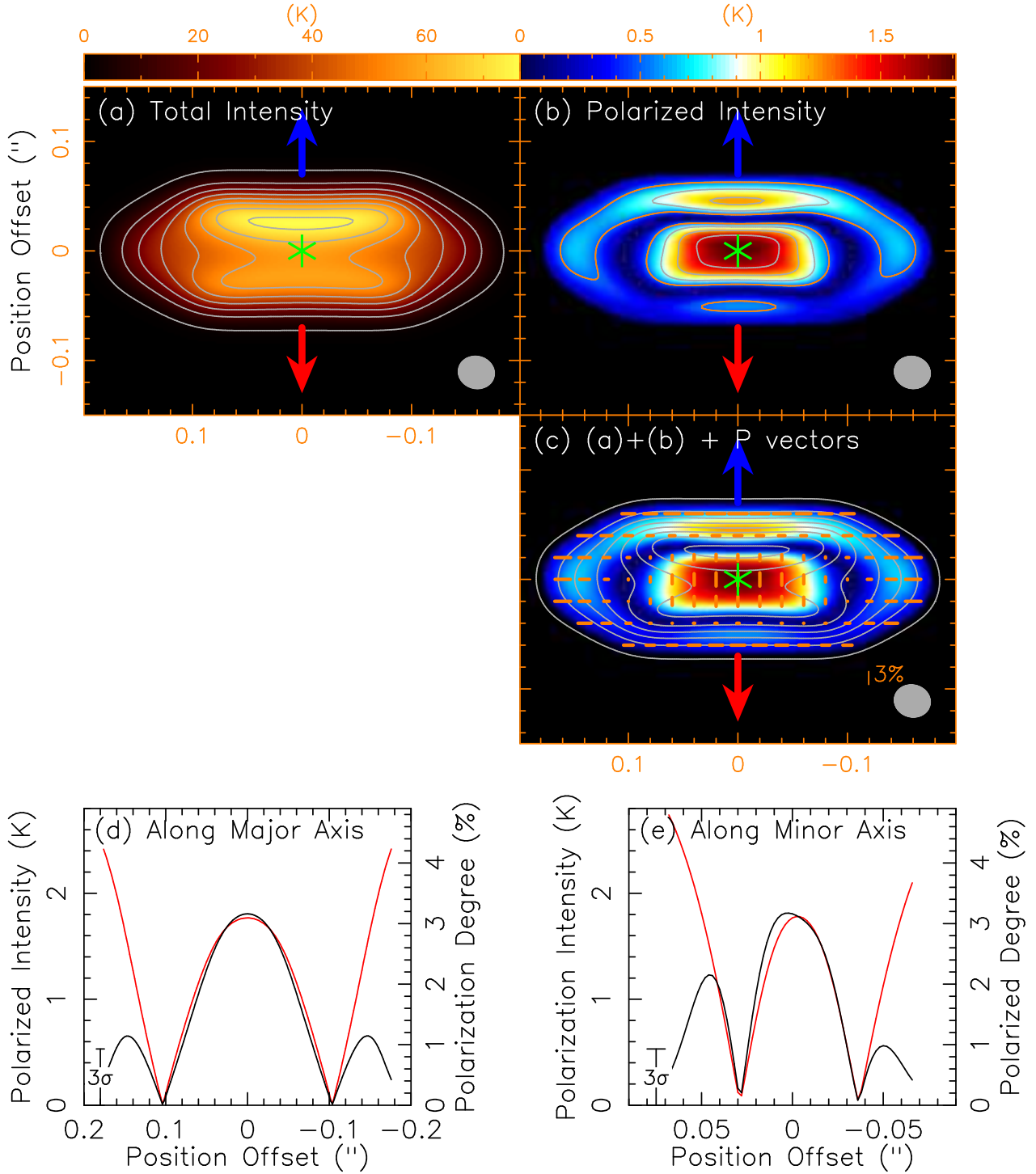


Fig. 4.— Same as Figure 3 but convolved to the observed beam to be compared with the observations. The contour levels in (a) and (c) are the same as those in Figure 1a. The contour levels in panel (b) are the same as those in Figure 1b, with the lowest contour (orange) showing the 3σ sensitivity level in our observations.

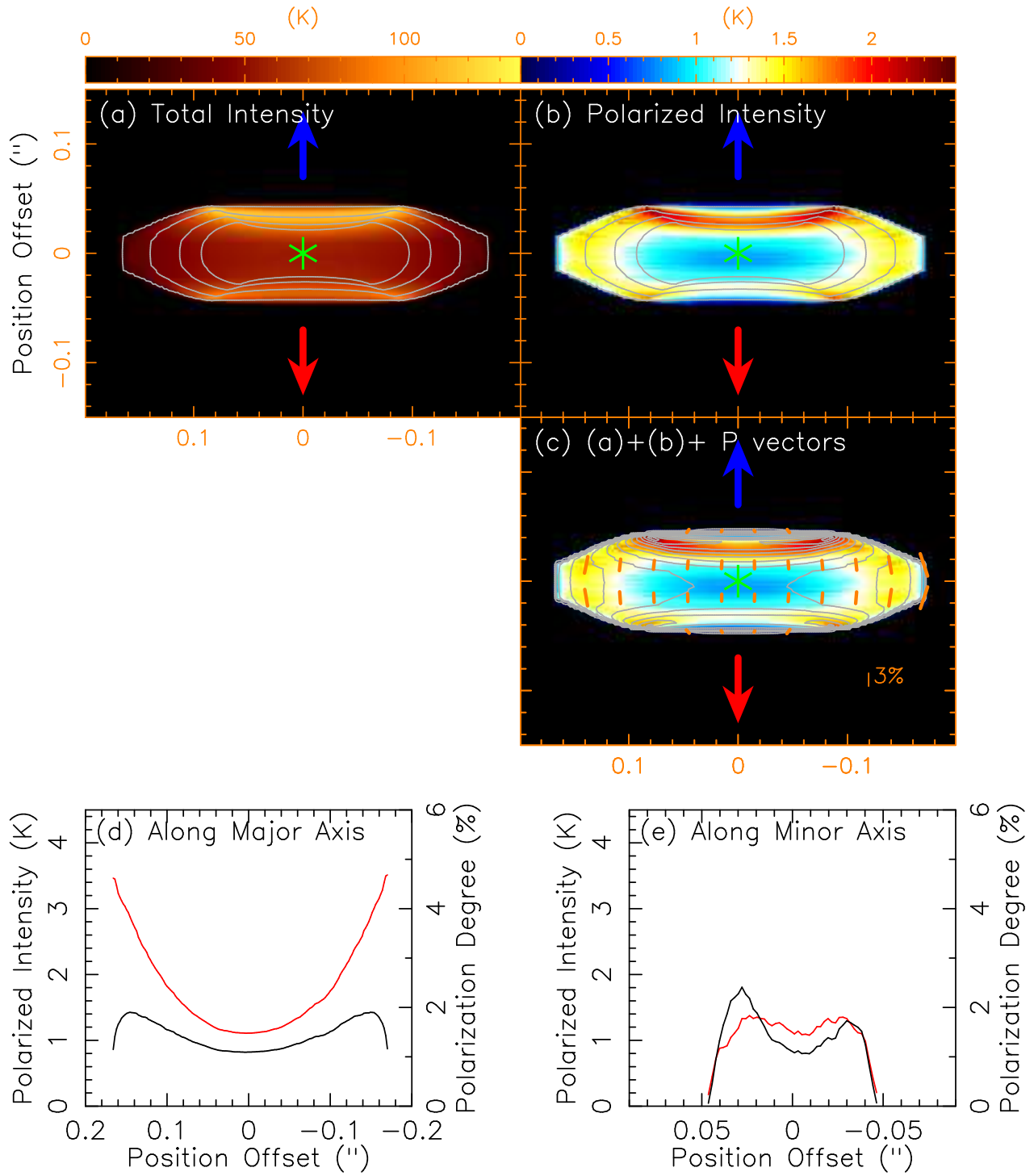


Fig. 5.— Dust self-scattering model. Same as Figure 3.

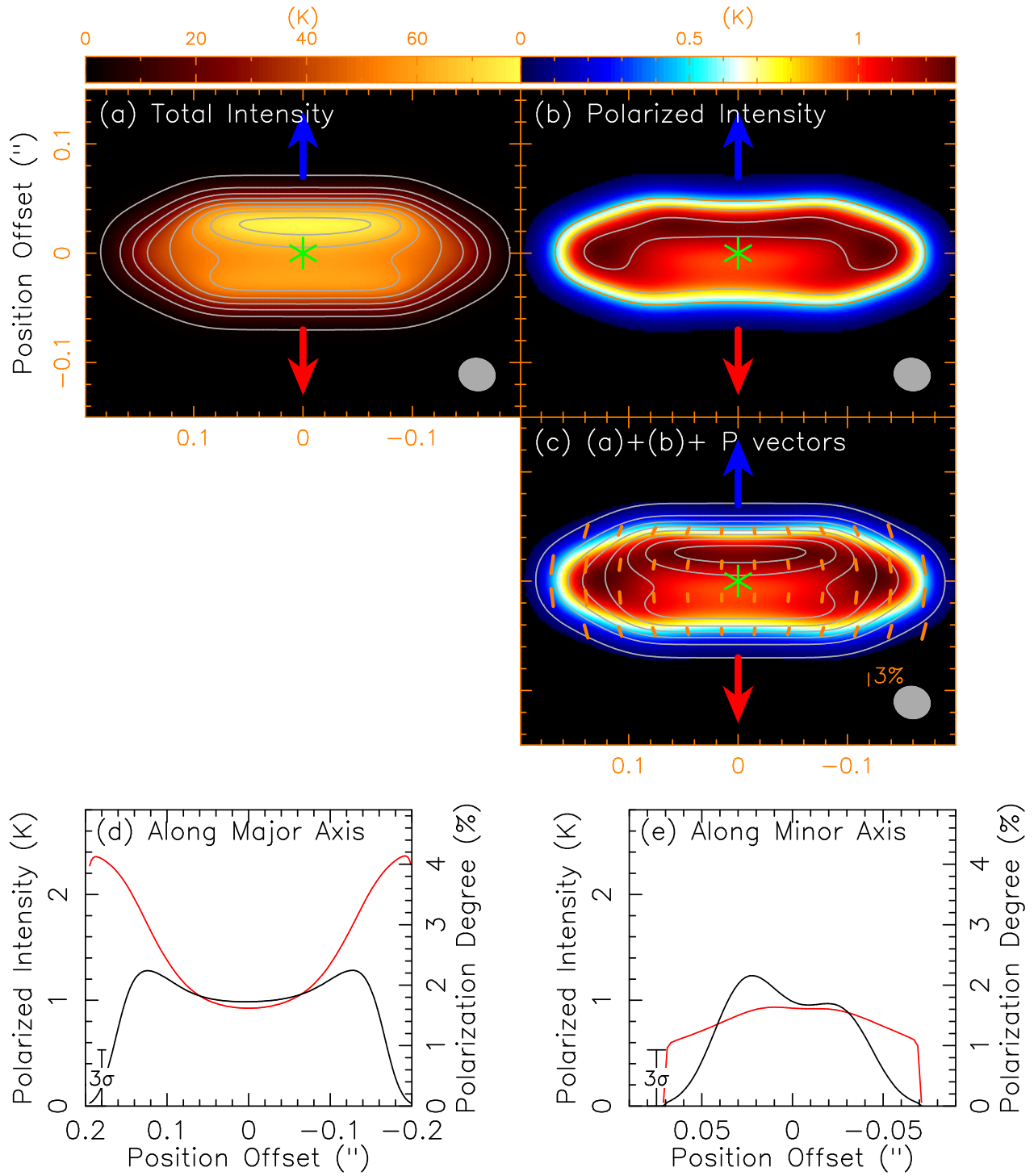


Fig. 6.— Same as Figure 5 but convolved to the observed beam to be compared with the observations. The contour levels are the same as those in Figure 4.